



HAL
open science

Synchrotron X-ray imaging in 4D: Multiscale failure and compaction localization in triaxially compressed porous limestone

Lingcao Huang, Patrick Baud, Benoit Cordonnier, François Renard, Lin Liu, Teng-Fong Wong

► To cite this version:

Lingcao Huang, Patrick Baud, Benoit Cordonnier, François Renard, Lin Liu, et al.. Synchrotron X-ray imaging in 4D: Multiscale failure and compaction localization in triaxially compressed porous limestone. *Earth and Planetary Science Letters*, 2019, 528, pp.115831. 10.1016/j.epsl.2019.115831 . hal-02334959

HAL Id: hal-02334959

<https://hal.science/hal-02334959>

Submitted on 21 Dec 2021

HAL is a multi-disciplinary open access archive for the deposit and dissemination of scientific research documents, whether they are published or not. The documents may come from teaching and research institutions in France or abroad, or from public or private research centers.

L'archive ouverte pluridisciplinaire **HAL**, est destinée au dépôt et à la diffusion de documents scientifiques de niveau recherche, publiés ou non, émanant des établissements d'enseignement et de recherche français ou étrangers, des laboratoires publics ou privés.



Distributed under a Creative Commons Attribution - NonCommercial 4.0 International License

1 **Synchrotron X-ray imaging in 4D: Multiscale failure and compaction**
2 **localization in triaxially compressed porous limestone**

3 Lingcao Huang^a, Patrick Baud^{b*}, Benoit Cordonnier^{c,d}, François Renard^{c,e}, Lin Liu^a,
4 Teng-fong Wong^a

5 ^a *Earth System Science Programme, Faculty of Science, The Chinese University of Hong Kong, Hong*
6 *Kong*

7 ^b *Institut de Physique du Globe de Strasbourg (UMR 7516 CNRS, Université de Strasbourg/EOST,)*
8 *France (patrick.baud@unistra.fr)*

9 ^c *Departments of Geosciences and Physics, The Njord Centre, University of Oslo, Norway*

10 ^d *ESRF, The European Synchrotron, CS40220, Grenoble 38043, France*

11 ^e *Univ. Grenoble Alpes, Univ. Savoie Mont Blanc, CNRS, IRD, IFSTTAR, ISTerre, 38000 Grenoble,*
12 *France*

13
14
15
16
17

18 **ABSTRACT**

19 Understanding failure and strain localization in porous rock is of fundamental importance in rock
20 physics. Confined compaction experiments on porous rocks have revealed a broad spectrum of
21 failure modes. Techniques such as acoustic emission location and velocity tomography provide
22 kinematic information on the partitioning of damage and localization of strain. Complementary
23 observations on deformed samples using microscopy and microcomputed tomography (μ CT) can
24 also be used to image microscale damage and its distribution. Only by synthesizing such
25 measurements on multiple scales could one infer the multiscale dynamics of compaction
26 localization and similar rock failure phenomena. Located at the European Synchrotron Radiation
27 Facility, the HADES rig allows direct *in situ* 3D imaging of the whole rock sample as it is
28 triaxially compressed. The μ CT data provide an integrated perspective of the spatiotemporal
29 evolution of damage and strain localization on scales ranging from grain to continuum. We
30 conducted an experiment on Leitha limestone (initial porosity of ~22%) at a confining pressure

31 of 20 MPa. With increasing differential stress, the sample strain hardened and two distinct yield
32 points were identified in the stress-strain curve. The spatiotemporal evolution of local porosity
33 and damage were analyzed at multiple scales. At a mesoscopic scale of 10 voxels (65 μm), the
34 time-lapse μCT images reveal the strain partitioning associated with the first yield point and
35 development of strain localization with the second. The latter development of five discrete
36 compaction bands is the first unambiguous observation of such a bifurcation phenomenon in a
37 porous carbonate rock, with geometric attributes comparable to compactions bands observed in
38 porous sandstones. The μCT data on the voxel-scale elucidate in refined details the nucleation
39 and propagation of discrete compaction bands under quasi-static loading, as well as the
40 micromechanical processes, which in the past can only be inferred from a synthesis of kinematic
41 observations of acoustic emissions activity and post-mortem observations of microstructure and
42 damage.

43

44 **Keywords:** limestone deformation, bifurcation, compaction bands, X-ray microtomography.

45

46 **1. Introduction**

47 Mechanical failure in the Earth's crust is often accompanied by localization of strain that
48 ranges in scale from hand specimens to zones of hundreds of kilometres. Crustal rock has pore
49 space made up of numerous elongate microcracks and equant pores. Under an applied stress field,
50 damage develops on the grain scale by growth of microcracks and collapse of pores. Initially
51 such damages proliferate in a distributed manner, but at higher stresses a subset may coalesce to
52 constitute a localized zone of intense deformation, which extends over multiple grains and
53 ultimately cuts through an experimental sample (e.g. Passchier and Trouw, 2005; Paterson and
54 Wong, 2005). In the field this process of strain localization cascades and extends in scale from
55 cm to hundreds of kilometres (Anders et al., 2015; Fossen et al., 2017).

56 Accordingly the phenomenon of strain localization is intrinsically a multiscale process, a
57 fundamental understanding of which hinges on integrated characterization of the spatiotemporal
58 development of damage from the grain to continuum scale. In a compact rock, compressive
59 failure typically involves brittle faulting accompanied by the localization of shear strain.
60 Acoustic emissions (AE) have been effective as proxies for the grain-scale damage related to
61 faulting. By locating the AE activity of a Westerly granite sample as it failed progressively under
62 quasistatic loading, Lockner et al. (1992) were able to elucidate the spatiotemporal development
63 of shear localization on the continuum scale. By analyzing the AE waveforms from multiple
64 receivers, one can broadly categorize the mechanism of an event as implosive, shear or tensile
65 (e.g., Zang et al., 2000), but further details of the grain-scale micromechanical processes can
66 only be acquired by systematic microscopy on the deformed samples (e.g., Wong, 1982; Moore
67 and Lockner, 1995).

68 In a porous rock compressive failure by brittle faulting is commonly observed, accompanied
69 also by shear localization. However, field and laboratory studies in the past two decades have
70 documented a fundamentally different mode of strain localization in porous rocks under high
71 confinement. Failure in this mode derives from cataclastic compaction that localizes in a planar
72 structure (compaction band, CB) oriented sub-perpendicular to the maximum compressive stress
73 (Mollema and Antonellini, 1996; Olsson, 1999). These CBs may develop as multiple discrete
74 bands (Wong et al., 2001; Baud et al., 2004), or as a diffuse band that widens with progressive
75 deformation (Olsson and Holcomb, 2000). In the laboratory, compaction band formation is
76 accompanied by significant permeability reduction (Vajdova et al., 2004; Baud et al., 2012),
77 whereas field observations and numerical simulations have highlighted potentially significant
78 impacts on fluid flow at the reservoir and aquifer scale (e.g., Sternlof et al., 2004).

79 Some of the most comprehensive investigations in the field and laboratory of this
80 phenomenon of compaction localization have been on porous sandstone (Fortin et al., 2005;
81 Tembe et al., 2008; Eichhubl et al., 2010; Fossen et al., 2011). Again AE measurements in the
82 laboratory have been effective in mapping out the spatiotemporal development of both discrete
83 and diffuse CBs (Olsson and Holcomb, 2000; Fortin et al., 2006; Townend et al., 2008). Only
84 when these kinematic data on damage development on the continuum scale are synthesized with
85 microstructural observations including X-ray computed tomography (CT) in 3D imaging (Louis
86 et al., 2006; Baud et al., 2015), can one arrive at a consistent description of the multiscale
87 mechanics of compaction localization. Ideally one would like to be able to acquire data on
88 multiple scales on a single sample, so as to resolve details on the dynamical development. How
89 did a CB nucleate and what micromechanical processes trigger the bifurcation in strain? It is
90 likely that the nucleation is from a preexisting local heterogeneity in the pore space or rock

91 matrix. What is the scale of the heterogeneity? For Bleurswiller sandstone Fortin et al. (2006)
92 inferred from their AE and CT data that relatively large heterogeneities in the form of “porosity
93 patches” provided nucleation sites for CBs, but Baud et al. (2015) argued that there is no causal
94 relation between collapse of these patches and CB formation.

95 In comparison, compaction localization in other porous rocks has not been investigated in as
96 much detail. In carbonate rocks, diffuse CBs have been reported in laboratory deformed samples
97 of calcarenite (Baxevanis et al., 2006) and Leitha limestone (Baud et al., 2017a). Microstructural
98 signatures of strain localization in porous limestones are subtle and not readily resolved under
99 either optical or electron microscopes (Ji et al., 2015). The use of AE for monitoring damage
100 development is limited by the typically low AE activity in calcitic rock (Vajdova et al., 2004;
101 Schubnel et al., 2006). Nevertheless, for the Saint-Maximin limestone Baud et al. (2017b)
102 observed significant AE activity likely related to microcracking at the quartz grain interfaces, but
103 according to microstructural observations, the dominant micromechanical process for
104 compaction was pore collapse, which seemed to be ineffective in generating AE. Spatial
105 distribution of AE in this quartz-rich limestone underscores the development of “complex diffuse
106 compaction bands” at high confinement. Accordingly these observations seem to indicate that
107 CBs in a carbonate rock tend to develop in a diffuse manner, which leads to the following
108 question: Can discrete CBs develop in a carbonate rock, and if not, what are the microstructural
109 attributes that inhibit their development?

110 The use of time-lapse 3D imaging by X-ray CT has opened up the possibility of
111 characterizing in situ the compressive failure of geomaterials (Lenoir et al., 2007; Andò et al.,
112 2012; Fusseis et al., 2013; Zhao et al., 2018). In particular, Renard et al. (2016, 2017) recently
113 developed a triaxial deformation apparatus that is transparent to the high flux of X-rays of a

114 synchrotron, which can potentially elucidate the multiscale failure of a crustal rock under
115 elevated pressures and temperatures. With a spatial resolution of several microns, the apparatus
116 furnishes 4D imaging of a centimeter-size sample loaded quasistatically in triaxial compression,
117 which delineates the progressive development of failure and strain localization from the grain to
118 continuum scale. In this study we leverage this advance in experimentation to tackle the several
119 questions outlined above, in relation to the development of compaction localization in the Leitha
120 limestone.

121

122 **2. Materials and Methods**

123 A cylindrical core (5 mm in diameter and 10 mm in height) of Leitha limestone was cored
124 orthogonal to the sedimentary bedding from a block collected in the quarry Hummel St.
125 Margarethen/ Burgenland near Vienna (Austria). The Leitha limestone is a carbonate grainstone
126 composed of > 99% calcite, and occurs with a broad range of grain sizes and porosity, related to
127 changes in depositional regime and degree of cementation (Rath et al., 2011). Baud et al. (2017b)
128 performed detailed microstructural analysis and X-ray CT imaging on samples with porosity
129 between 18% and 31%. They showed that Leitha limestone is essentially an aggregate of
130 cemented bioclasts of relatively homogeneous size, and the pore space of samples from our
131 block is dominated by macropores of relatively large size (with average around 165 μm).

132 Several other samples were cored for porosity measurement and additional mechanical tests.
133 With a helium pycnometer the porosity of a sample (20 mm in diameter and 40 mm in height)
134 that had been dried *in vacuo* for 48h was determined to be 26%, in agreement with another

135 estimation based on the bulk density of the sample and assuming that the studied rock is made of
136 100% of calcite.

137 The experiment was conducted at the European Synchrotron Radiation Facility (ESRF) in
138 Grenoble, France, using the triaxial compression apparatus, HADES (Renard et al., 2016)
139 installed on an X-ray μ CT rotation stage at beamline ID19. The sample was jacketed with Viton,
140 and confining medium was silicon oil. A confining pressure up to 100 MPa can be generated,
141 with a maximal uncertainty of 0.05 MPa. The differential stress up to a maximum value of 200
142 MPa was independently applied. The axial displacement was monitored with a displacement
143 transducer (LVDT), with a precision of 3 μ m.

144 The experiment was conducted on the nominally dry sample at room temperature. A
145 hydrostatic stress of 20 MPa was first applied, and before the application of differential stress,
146 the first X-ray tomography scan was acquired. Made of titanium, the body of the triaxial rig is
147 transparent to X-rays from the synchrotron source (with estimated equivalent beam energy of 85
148 keV). Keeping confining pressure fixed at 20 MPa, the axial piston was progressively advanced
149 by increments of 1-2 MPa. After each step in stress, the differential stress was held constant as
150 the apparatus was rotated over 180°, while 1,800 X-ray radiographs were acquired with a voxel
151 size of 6.5 μ m. The radiograph extended over 13x13 mm² (2000x2000 voxels), covering full
152 length and width of sample and parts of the pistons and confining medium. Durations of the
153 stress step and tomography scan were 1-2 minutes and 3 minutes, respectively. Reconstruction of
154 the 3D volumes from the radiographs was performed at beamline ID19 at the ESRF, using both
155 X-ray adsorption and phase contrast imaging (Mirone et al., 2014).

156 First-order characteristics of the pore space can be inferred from the global histogram of the
157 X-ray attenuation coefficient mapped onto a gray level. Fig. S1 shows the 16-bit data for our
158 limestone sample at differential stresses of 4, 55 and 74 MPa. In each histogram one can readily
159 recognize two distinct modes, with relatively symmetric distributions on either side of the peaks.
160 The area under the first peak decreases with increasing compaction. The two modes are
161 separated by a broad range of gray level, with a well-defined intermodal valley in between.
162 Guided by our previous microstructural observations (Baud et al., 2017a) and macroscopic
163 measurement of porosity, we binarized the CT-images by selecting a fixed gray level (9500) as
164 the threshold for segmentation, such that the void and solid domains correspond to voxels with
165 gray levels below or above this threshold. It should be noted that we were able to adopt this
166 simple protocol for segmentation only because the pore space of our Leitha limestone sample
167 was dominated by macropores, with minimal microporosity. In most limestones with significant
168 fractions of dual porosities, the intermodal valley is not as well-defined, and more elaborate
169 protocols are necessary for segmentation (Ji et al., 2012).

170

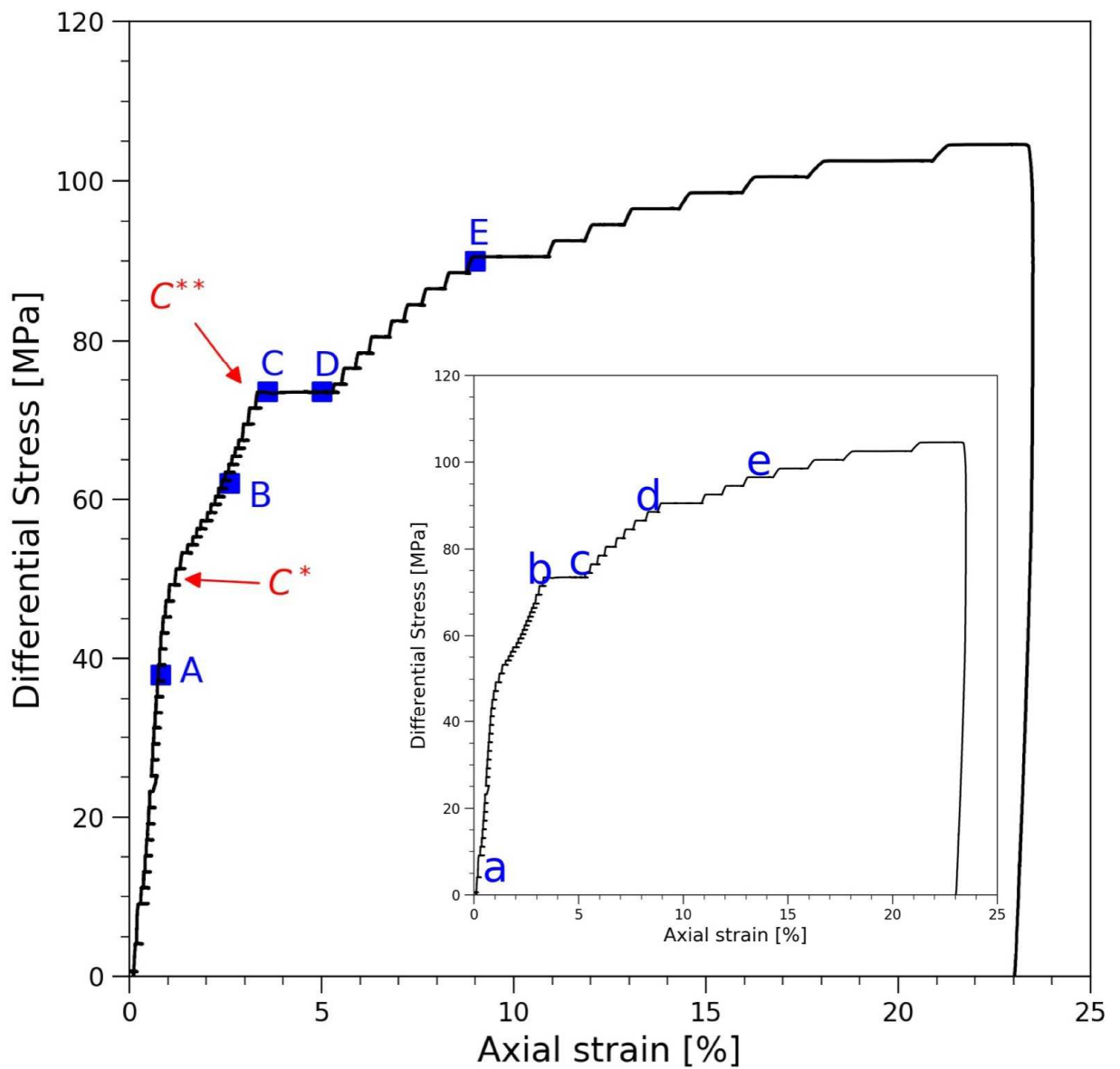
171 **3. Results**

172 *3.1. Mechanical deformation and failure mode*

173 We present in Fig. 1 the mechanical data, with the differential stress as a function of axial
174 strain (shortening measured from LVDT divided by the nominal sample length). The differential
175 stress increased monotonically to a level of 104 MPa, as the sample accumulated an axial strain
176 of more than 20% before it collapsed catastrophically. Two notable changes in the slope of the
177 stress-strain curve were observed at differential stresses of 50 MPa and 73 MPa, marked by C^*

178 and C^{**} in the Fig. 1, respectively. We will argue later that the sample underwent two stages of
179 yielding associated with these two critical stresses. We also present videos S2 and S3, which are
180 time-lapse radiographs of two orthogonal axial sections (R0 and R90) of the sample acquired in
181 the experiment.

182



183
184
185

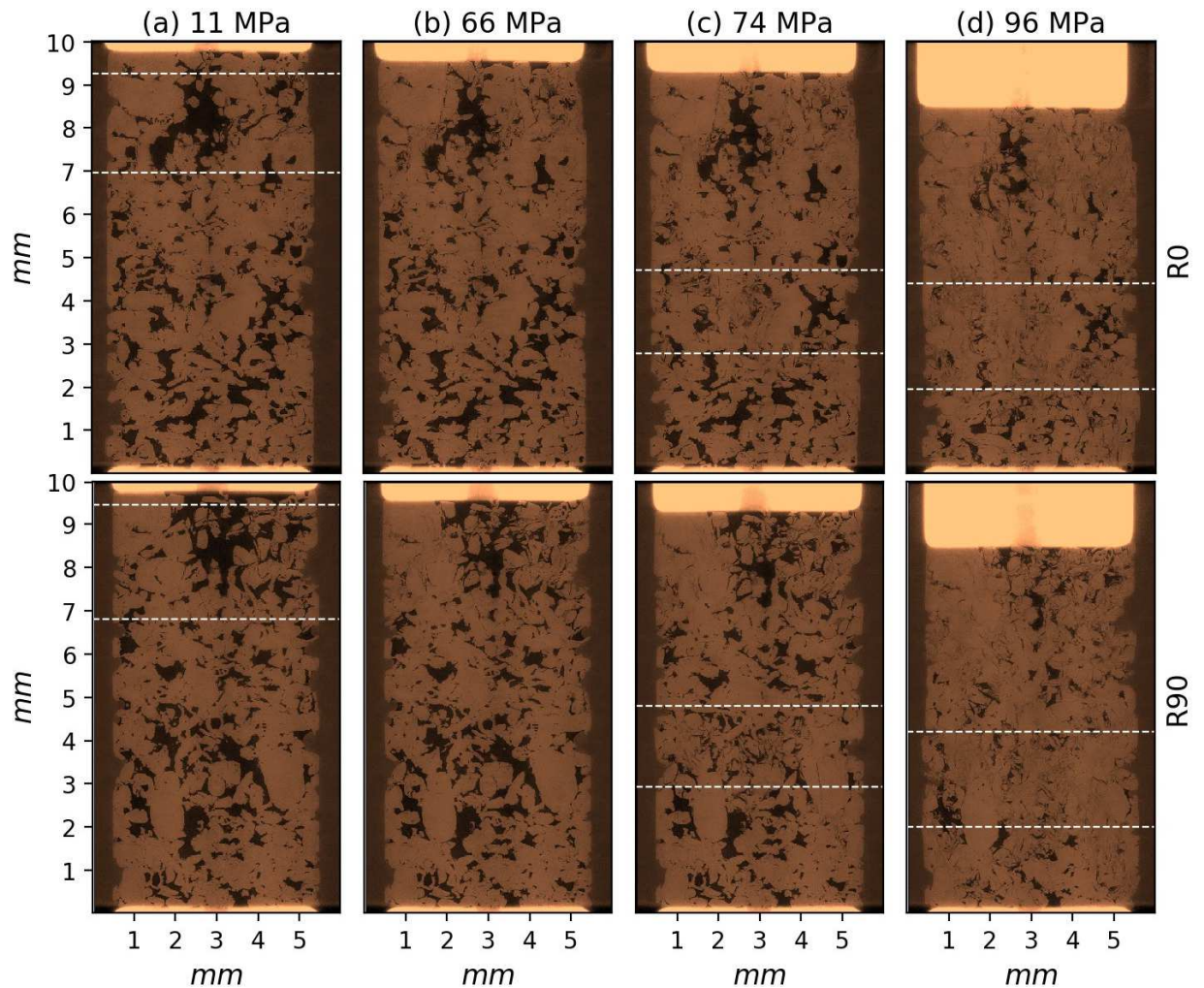
186
187
188
189
190
191
192
193

Fig. 1. Mechanical data for a sample of Leitha limestone deformed at a confining pressure of 20 MPa. Differential stress is plotted as a function of axial strain. The critical stresses C^* and C^{**} are indicated by red arrows. The steps (A, B, C, D, E) for the five scans in Fig.4a are marked on the stress-strain curve. Similarly the steps (a, b, c, d, e) for the micrographs in Fig.7, Fig.8 and Fig. 9 are marked on the inset stress-strain curve.

The radiographs at four stress levels were selected to highlight the progressive development of damage as seen in the videos. At a low differential stress of 11 MPa (and confining pressure of 20 MPa), the sample sustained mostly elastic deformation and its pore space is likely similar to the undeformed state. The orthogonal radiographs (Fig. 2a) show that this initial distribution of porosity was quite heterogeneous, and in particular, a large cluster of macropores can be seen within a top layer (bracketed by the two white dashed lines). At a stress of 66 MPa (well beyond C^* but before C^{**}), this macropore cluster and other pores in the top layer have compacted significantly. Nevertheless deformation in this layer appears distributed, in that the large and small pores both seem to have sustained comparable compaction. In contrast, the lower two-third of the sample showed minimal compaction (Fig. 2a and 2b).

Fig. 2c was acquired at a stress of 74 MPa after the sample had sustained an overall strain of ~2% beyond C^{**} . Most of the pores had contracted to a degree, but the most intense compaction developed preferentially within a layer bracketed by the white dashed lines in the lower half of the sample. As the sample strain hardened to a stress of 96 MPa and accumulated an overall strain of 15%, compaction appeared to have preferentially developed in a somewhat thicker layer (bracketed by white lines in Fig. 2d). If these were the only micrographs of the deformed sample available, the likely interpretation would be that these layers in Fig. 2c and 2d correspond to the widening of a diffuse CB. However, our latter analysis will reveal that this interpretation is overly simplistic. It should also be noted that our sample at the highly deformed stages did not

212 show any sign of asymmetric bulging, which would have indicated the development of shear
213 localization.



214
215 **Fig. 2.** Radiographs of two orthogonal sections (R0 and R90) at (a) 11, (b) 66, (c) 74, and (d) 96
216 MPa of differential stress.

217
218 *3.2. Strain partitioning and compaction localization*

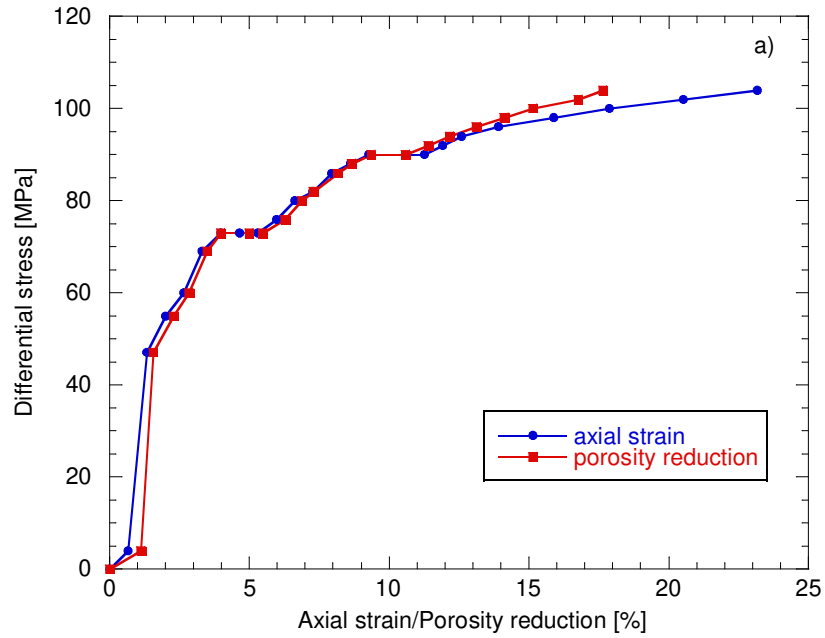
219 The 4D imaging allows us to characterize the deformation from the sample scale down to
220 voxel scale. This is tackled first using the segmented images. With reference to the grayscale
221 threshold (Fig. S1), all the CT images were segmented into solid and void domains. The standard
222 protocol in microstructural analysis is to exclude regions in the vicinity of the jacket and loading

223 pistons, to circumvent artifacts induced by local stress anomalies and end effects. We adopted
224 the same approach, masking such regions in our analysis. The diameter was reduced from 5 mm
225 to 4.55 mm (700 voxels) in the masked segmented images. Two layers of thickness 0.13 mm (20
226 voxels) were masked in the immediate vicinity of the top and bottom pistons, respectively.

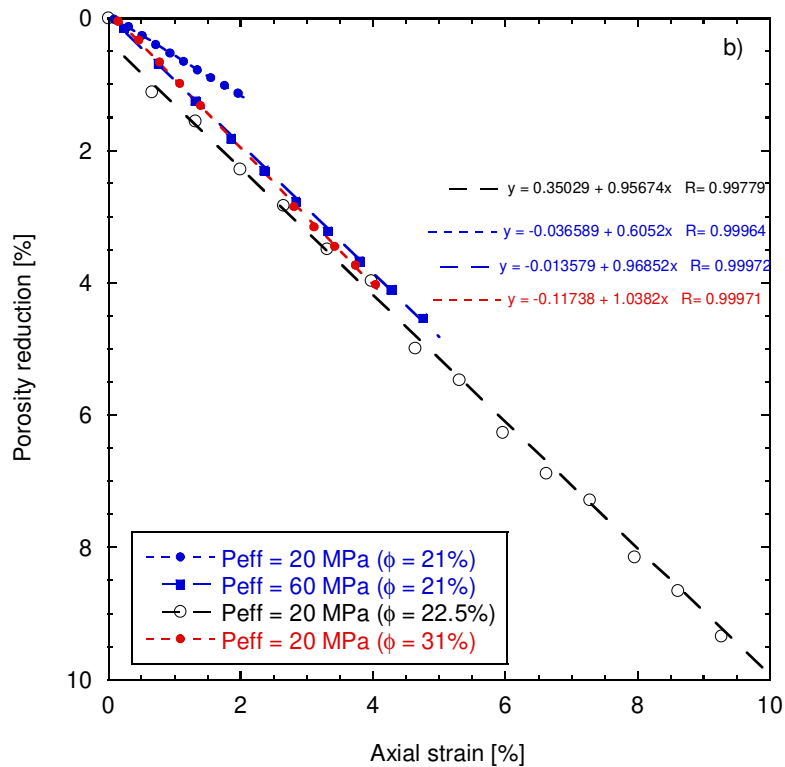
227 At the sample scale the porosity ϕ of our segmented CT images had an initial value of 22.5%
228 at confining pressure of 20 MPa. As noted earlier the porosity of a larger sample under ambient
229 pressure was determined to be 26%, and the apparent discrepancy can be attributed to several
230 factors. First is compaction due to the hydrostatic confinement. Second, a disproportionate
231 number of macropores were observed in the masked region near the sample ends and surface,
232 which were excluded in our analysis. Third, there could be pores smaller than the voxel
233 dimension of 6.5 μm not resolved in the μCT images.

234 The peak differential stress attained in the experiment was 104 MPa, and by then most of the
235 porosity was eliminated down to 4.8% (Fig. 3a). On the μCT images we can determine the axial
236 shortening from the change in piston positions and divide it by the initial length, thus arriving at
237 an independent measure of the axial strain ϵ , which is plotted in Fig. 3a and shown to be in good
238 agreement with the LVDT data in Fig. 1. Interestingly our data show that the porosity reduction
239 $\Delta\phi$ and axial strain ϵ basically coincided during most of the experiment up to about 15% of axial
240 strain, with the implication that although the limestone sample was compressed triaxially,
241 negligible deformation developed in the transverse direction such that the axial strain was
242 essentially taken up by a corresponding reduction in porosity. The absence of dilatancy during
243 triaxial compression also suggests that dilatant failure by shear faulting was unlikely. According
244 to bifurcation analysis of strain localization, such a deformation field is favorable for CB

245 formation (Rudnicki, 2004). Baud et al. (2004) also showed that CBs in Bentheim sandstone
246 developed with negligible radial strain.



247



248
 249 **Fig. 3.** (a) Differential stress as a function of axial strain (blue) and porosity reduction (red), both
 250 calculated from the CT images, for the sample deformed in this study at a confining pressure
 251 of 20 MPa. (b) Compilation of data on Leitha limestone. Porosity reduction is plotted as a
 252 function of axial strain for samples of starting porosity 21% (red), and 31% (blue) deformed
 253 by Baud et al. (2017a) in wet conditions at different effective pressures P_{eff} (i. e. the difference
 254 between the confining pressure and the pore pressure).
 255

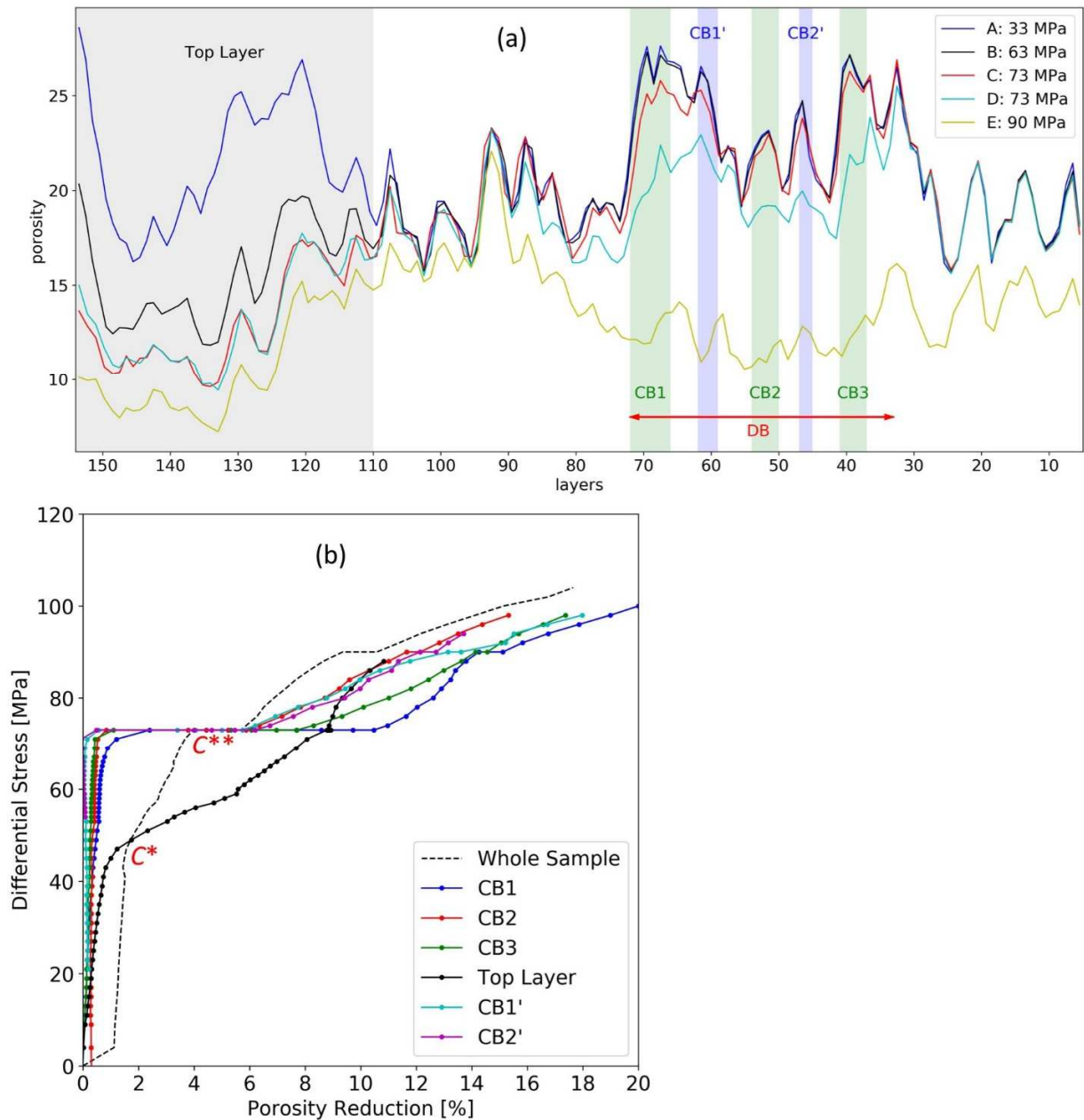
256 It should be noted that previous experiments on Leitha limestone (Baud et al., 2017a) have
 257 reported a linear relation $\Delta\phi = k\varepsilon$ between the axial strain and porosity reduction over a broad
 258 range of conditions. For reference we include in Fig. 3b selected published data on Leitha
 259 limestone for porosity reduction versus axial strain. Water-saturated samples of initial porosity
 260 21 and 31% were deformed in drained conditions over a wide range of effective pressures P_{eff}
 261 (i.e. the difference between the confining pressure and the pore pressure). In these experiments,
 262 $\Delta\phi$ was calculated from the ratio of the pore volume change, inferred from the monitoring of the
 263 pore pressure, to the initial bulk volume of the samples (see Baud et al., 2017a for details). There
 264 is a trend for the slope k of the data presented in Fig. 3b to increase with increasing effective

265 pressure. For example, for the samples of 21% initial porosity k increased from 0.61 at an
266 effective pressure of 20 MPa to 0.97 at an effective pressure of 60 MPa. It should be emphasized
267 that the global relation $\Delta\phi = k\varepsilon$ applies independent of the failure mode. In particular, since
268 some of these samples have developed CBs and strain localization, this implies that the relation
269 likely applies also to the local porosity and strain at the mesoscopic scale. Such data can
270 accordingly be used to calibrate the partitioning of porosity change (from CT imaging) between
271 axial and transverse strains. In our study, it is particularly simple in that porosity change and
272 axial strain are equal, with negligible transverse strain.

273 To analyze the strain partitioning at the mesoscopic scale, we divided the initial sample into
274 156 layers with a thickness of 65 μm (10 voxels), and determined the local porosity of each layer
275 from the segmented CT image. Such an approach is like treating each layer as a representative
276 element volume at the mesoscopic scale, and the local porosity here corresponds to an average
277 over the volume of each layer. In an experimental context, this is analogous to performing
278 porosimetry measurements on more than one hundred locations in the sample. In the experiment
279 the sample shortened by as much as 20% (Fig. 1); so that we can compare the strains at fixed
280 particle points, we determined the local porosity change $\Delta\phi$ between two scans in each layer,
281 equated it to the local axial strain ε , and then expanded the layer thickness by a factor of $1/(1-\varepsilon)$.
282 This would dilate and adjust the current length of a deformed sample that of the initial sample for
283 comparison.

284 We plot in Fig. 4a the local porosity as a function of the adjusted length at five selected
285 stress states marked (A, B, C, D, E) on Fig. 1. Between A and B, the differential stress increased
286 from 33 MPa to 63 MPa (beyond the first yield point C^*). Comparison of the two profiles

287 underscores that compaction was unevenly partitioned between the upper and lower parts of the
288 sample. It preferentially developed in a top layer (shaded in gray, corresponding to the cluster of
289 macropores marked in Fig. 2a), where the porosity decreased overall by ~7%. Below this layer,
290 little change of local porosity was observed. Although compaction was significant within the top
291 layer, its porosity profile remained qualitative similar in that six corresponding peaks can be
292 identified in profiles A and B. The absence of compaction localization confirms that the yielding
293 at C^* was associated with the preferential development of distributed compaction in the top
294 layer.



295
 296 **Fig. 4.** (a) Local porosity as a function of the μ CT layer number in the deformed sample at five
 297 stress states (A,B,C,D,E) marked in Fig. 1. The gray shaded area corresponds to the cluster of
 298 macropores marked in Fig. 2a. Five compaction bands, CB1, CB2, CB3, CB1' and CB2' are
 299 indicated on the graph as green and purple areas. These bands coalesced to form the diffuse
 300 compaction band DB indicated by the red arrow. (b) Porosity reductions as function of
 301 differential stress for the five compaction bands. For comparison, the global porosity
 302 reduction and the porosity reduction in the top layer are also shown as black dashed and solid
 303 lines, respectively. For reference, the two yield stresses C^* and C^{**} are marked in red.
 304

305 The porosity profile C is for a stress of 73 MPa at the onset of the second yielding C^{**} .
306 Comparison of profiles B and C shows preferential compaction that persisted within the top
307 layer, with little change of local porosity in the rest of the sample, except for a layer CB1 with
308 appreciable reduction in porosity (Fig. 4a). In the transition from C to D, the sample crept for
309 several minutes and accumulated a global strain of $\sim 1\%$. Comparison of the two profiles before
310 and after C^{**} shows that compaction had completely shifted to the lower half of the sample, with
311 negligible change in porosity in the top layer. In particular, pronounced compaction had
312 preferentially developed in five layers: CB1 with thickness of 0.39 mm; CB2 and CB3, both of
313 thickness of 0.26 mm; and two relatively thin layers CB1' and CB2' (with thicknesses of 0.20
314 mm and 0.13 mm, respectively). This preferential development of localized porosity at the
315 mesoscopic scale suggests that yielding at C^{**} first triggered the nucleation of a discrete
316 compaction band CB1, and the creep deformation was subsequently accommodated by the
317 development of four more discrete bands (CB2, CB3, CB1', CB2'), also visible in the videos S2
318 and S3 presented in supplementary material.

319 Profile E was acquired at a stress of 90 MPa, when the sample had accumulated a strain of
320 $\sim 10\%$ (Fig. 1). Comparison with profile D indicates that a significant fraction of the compaction
321 was observed within the layer DB marked in Fig. 4a, which corresponds to the layer bracketed in
322 Fig. 2. A comparison of profiles A and E also shows that, towards the end of the experiment, the
323 initial heterogeneity in local porosity within layer DB had been smoothed out. The five discrete
324 CBs are embedded within this layer, and our interpretation is that these bands had coalesced to
325 form the diffuse compaction band DB.

326 To characterize quantitatively the partitioning of strain among the top layer and CBs, we
327 plot in Fig. 4b their porosity reduction as function of differential stress. For reference we include

328 the global porosity reduction and mark the two yield stresses. After the first yielding C^* and
329 before onset of the second yielding C^{**} , the top layer accumulated a local strain of 8%, which
330 represents a global strain of ~2%, comparable to that measured for the whole sample. This
331 corroborates the predominant contribution of the top layer towards compaction during this first
332 stage of yielding. As the sample crept at a stress of 73 MPa, the five bands CB1, CB2, CB3,
333 CB1' and CB2' had their local porosities reduced by 9%, 6%, 7%, 5% and 5%, respectively (Fig.
334 4b), which collectively contribute a global strain of about 1%. This constitutes about half of the
335 strain measured for the whole sample, although their thicknesses amount to only one-quarter of
336 the sample length.

337 As elaborated in the supplementary material, our high-frequency displacement data indicate
338 that, even though the stress level was kept at a nominally constant level during the creep stage, it
339 was actually punctuated by five relatively small stress drops (Fig. S4). We interpret that these
340 stress drops were associated with the nucleation and development of the five discrete CBs,
341 analogous to observations documented extensively in sandstones (Wong and Baud, 2012).

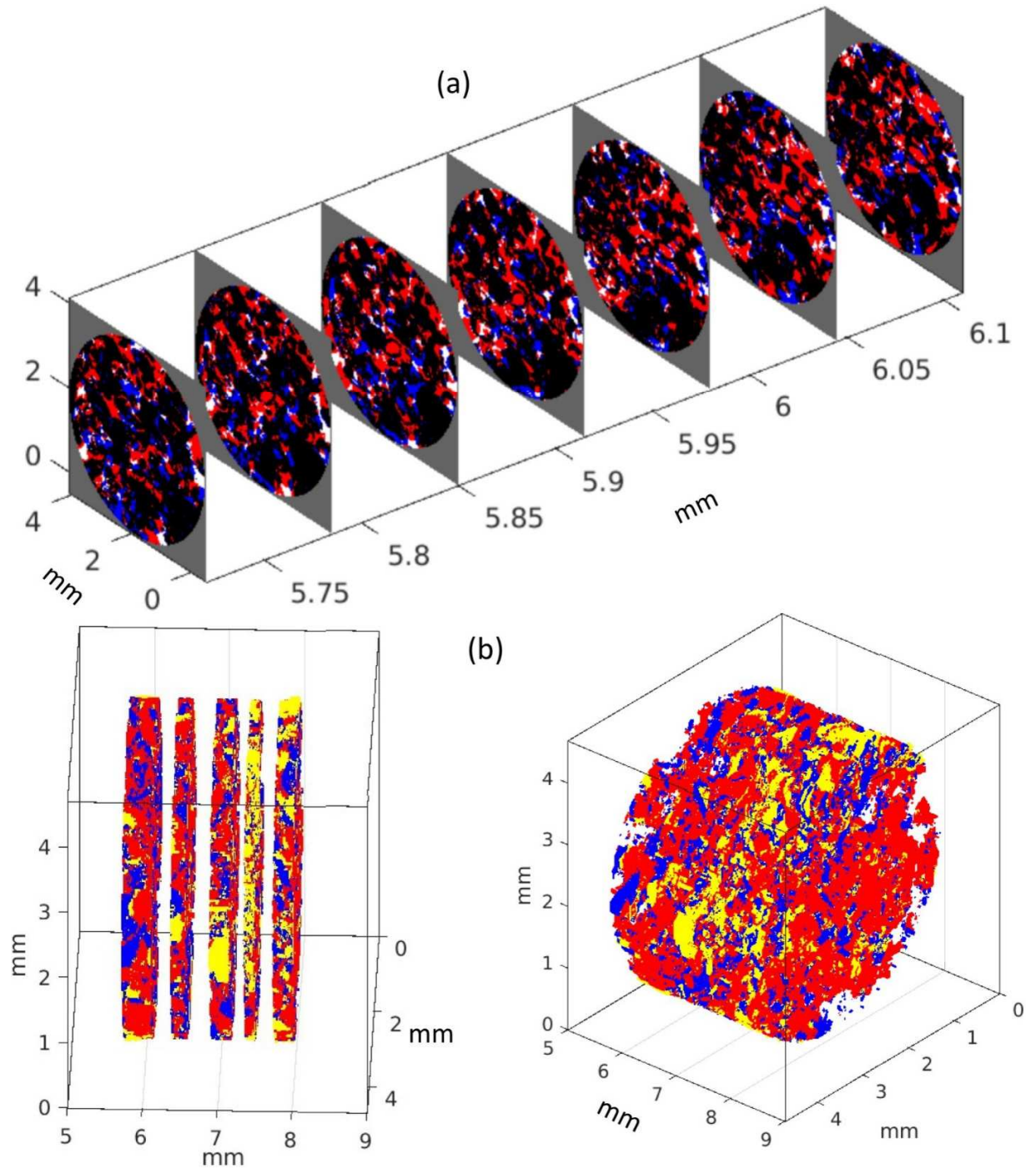
342 *3.3. Spatiotemporal development of damage and micromechanics of failure*

343 Having pinpointed five discrete CBs from our mesoscopic analysis, we next refined the
344 scale to the voxel to further elucidate the spatiotemporal development of these CBs and the
345 associated damage. To quantify the damage we compared two segmented CT images acquired
346 before and after a CB had initiated and propagated across the sample. Between the scans, the
347 deformation of a voxel falls into one of four distinct modes: (1) void to solid, (2) solid to void,
348 (3) solid remains solid, and (4) void remains void. Both modes 1 and 2 could occur only if a
349 voxel had been affected by damage and irreversible displacement. The stress levels and scan
350 numbers we selected for analyzing the five CBs are listed in Table T1 in supplementary material.

351 For each band, the percentages of voxels with deformation in either mode 1 or mode 2 were
352 evaluated (Table T1).

353 For the thickest band CB1, between the two scans (at differential stresses of 73 MPa and 82
354 MPa) the porosity decreased by ~10% (Fig. 4b) which, according to Table T1, corresponds to the
355 trade-off between (mode 1) compaction of 19.7% and (mode 2) dilation of 9.2%. This also
356 implies that altogether 28.9% by volume of CB1 was subjected to either modes of deformation, a
357 proxy for the spatial extent that had been impacted by either compactant or dilatant damage. It
358 should be noted that, because damage in the form of sub-micron microcracking cannot be
359 resolved by our μ CT imaging, this percentage likely represents only a lower bound of the
360 damage zone. To highlight the spatial heterogeneity and connectivity of damage, we present in
361 Fig. 5a seven slices along the width of CB1. The damage zone corresponds to the red and blue
362 areas. Our analysis of the spatial distribution and connectivity in the other four bands (Table T1)
363 show that they are qualitatively similar, as illustrated by the 3D images in Fig. 5b.

364 Whereas this refined analysis delineates details of the spatial distribution of damage on the
365 voxel scale, it has an intrinsic limitation in that little regarding the micromechanical processes is
366 revealed beyond whether they are either compactant or dilatant. Indeed a similar limitation
367 applies also to the measurement of AE as a proxy for damage. In this regard our approach has a
368 distinct advantage because details of the grain-scale deformation were also revealed in the gray-
369 scale images (Fig. 2). We first scrutinized the images at large deformation to track down features
370 that would suggest shear localization cutting through the sample. We were not able to detect
371 inklings of such a development. Focusing on selected regions, we next analyze the time-lapse
372 radiographs (R90) to track the sequential development of pore collapse and CB formation and to
373 infer the micromechanics.



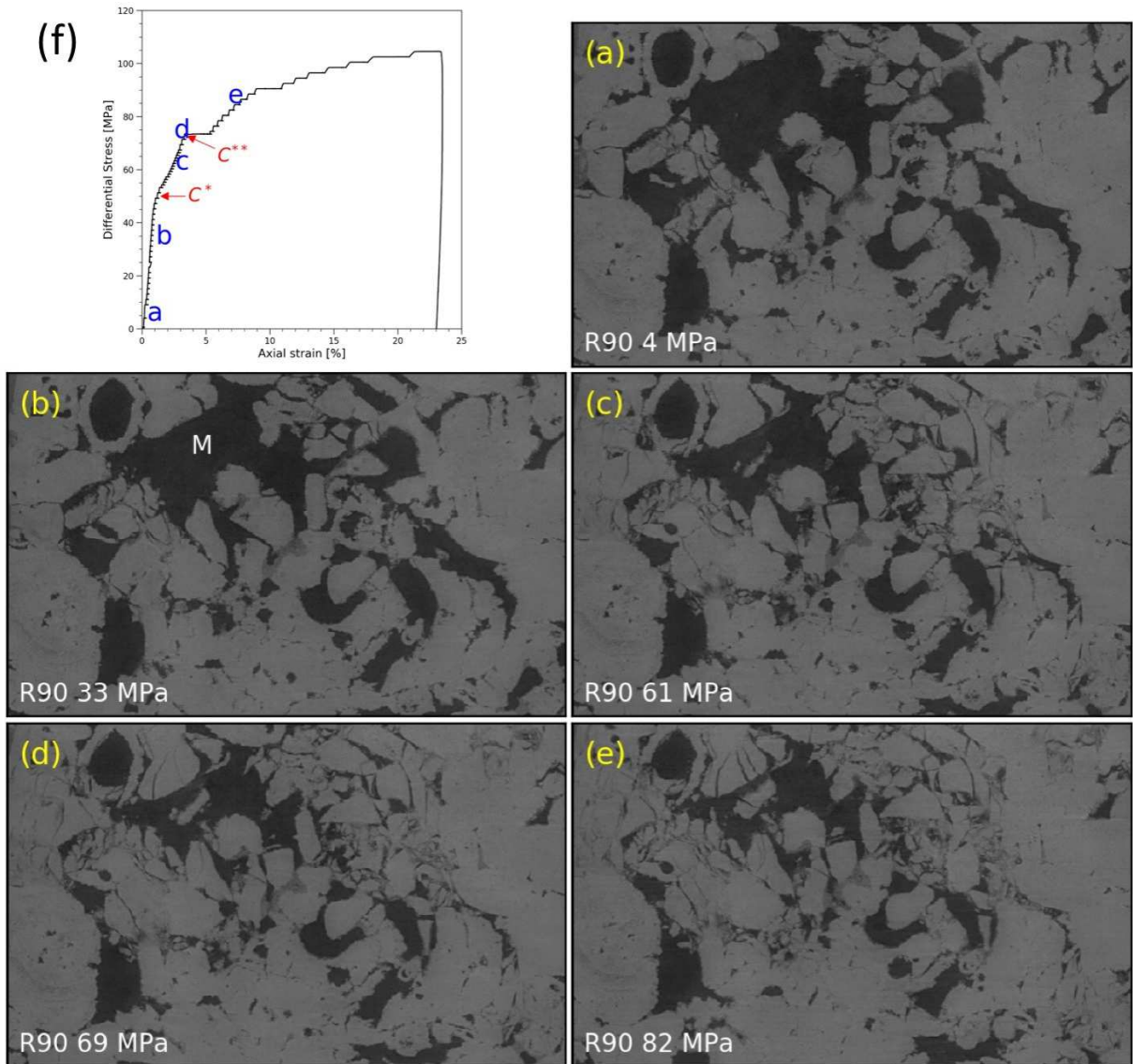
374
375

Fig. 5. (a) 3D visualization of damage and porosity reduction in CB1. Seven slices along the width of the band are shown. The voxel-scale deformation falls into four modes (1 compaction: red; 2 dilation: blue; 3 solid; black; 4 void: white). (b) 3D visualizations of damage in the

376
377

378 compaction bands. The voxel-scale deformation falls into four modes (1 compaction: red; 2
379 dilation: blue; 3 solid: yellow; 4 void: white).

380
381 Five time-lapse micrographs of the top layer are shown in Fig. 6. The letter code (a, b, c, d,
382 e) of these figures correspond to the stress states marked in Fig. 6f. Fig. 6a and 6b were acquired
383 at two stresses before C^* ; their pore spaces seem almost identical, underscoring that relatively
384 little deformation occurred before the first yield point C^* was reached. The macropore (marked
385 as “M” in Fig. 6b) stands out as one of the largest voids. When the stress increased beyond C^* ,
386 significant deformation can be observed (Fig. 6c), preferentially in the vicinity of M. Axial
387 shortening of this macropore was significant, and to accommodate this, compaction developed
388 on either sides of M in the form of grain crushing and collapse of the smaller pores. Where
389 grains impinged on one another, Hertzian fractures initiated and propagated across grains. When
390 a grain was crushed into fragments, some of them fell into the macropore. Beyond the stress state
391 c, the pores continued to contract somewhat, but it can also be seen from Fig. 6d and 6e that
392 compaction in this layer remained distributed.

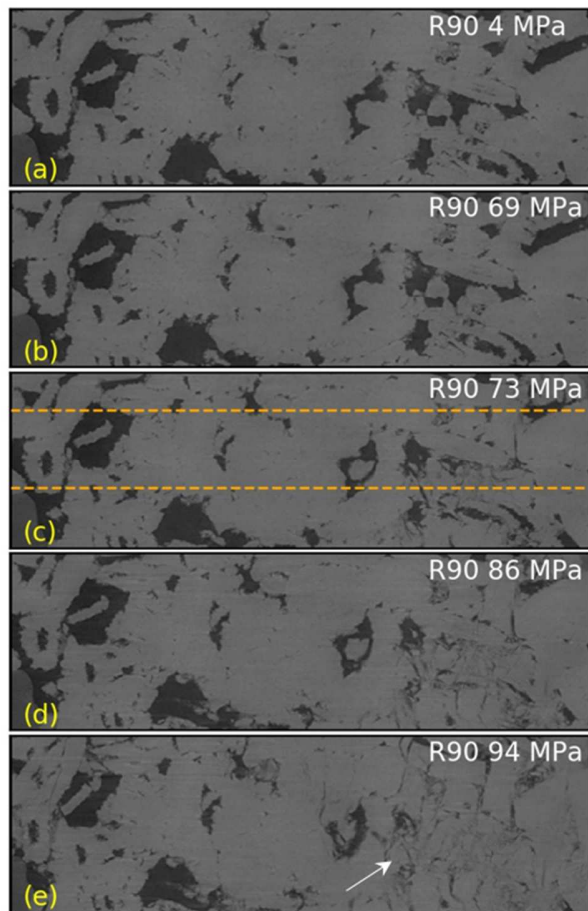


393
 394 **Fig. 6.** (a-e) Five micrographs of the top layer of the sample acquired at different levels of stress
 395 marked in (f). The width of the micrographs is 4.55 mm. The letter M labels a macropore.
 396

397 Five time-lapse micrographs of regions that embed CB1, CB2 and CB2 are presented in Fig.
 398 7, Fig. 8, and Fig. 9, respectively. The letter code in these figures correspond to the stress states
 399 (a, b, c, d, e) marked in the inset of Fig. 1. Fig. 7a and 7b were acquired at two stresses before
 400 C^{**} , and their pore spaces seem almost identical, showing that relatively little deformation
 401 occurred in this region before the second yield point C^{**} was reached. However, once C^{**} had
 402 been attained and the sample crept for several minutes, significant compaction was observed

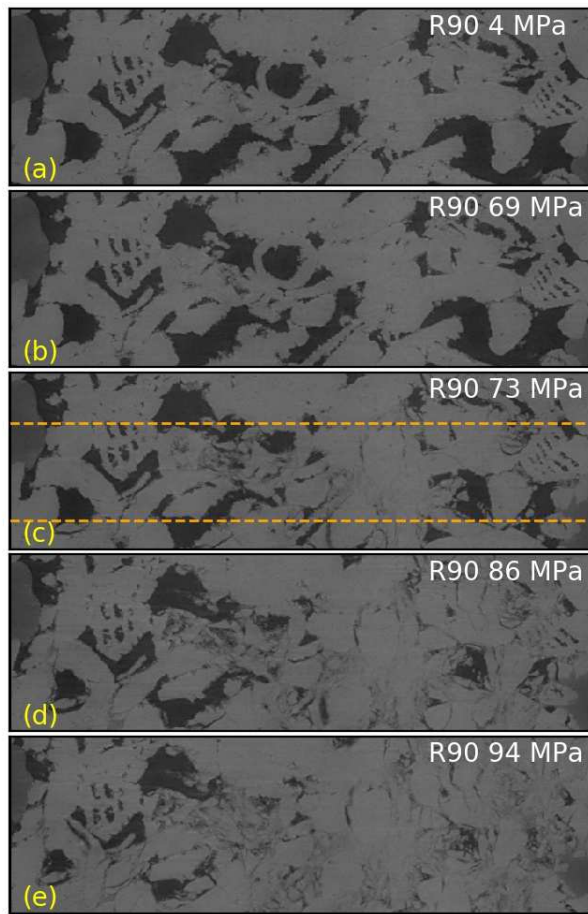
403 (Fig. 7c). Unlike what occurred in the top layer, deformation seemed not to have preferentially
404 developed near the larger pores. Many of the smaller pores had been eliminated, and larger pores
405 had also contracted appreciably. It is likely that grain crushing was pervasive, but the CT images
406 cannot resolve the details. The grain-scale damages were localized in a planar zone aligned along
407 CB1, and at this stage appeared more intense in the right half of the region bracketed by the two
408 dashed lines. In the next stage (Fig. 7d), the damage had spread towards the left as the sample
409 strain hardened. In the last micrograph (Fig. 7e), one can identify a band of damage that cuts
410 through about half of the sample.

411 In Fig. 8 and Fig. 9, damage evolutions in the other two bands CB2 and CB3 are
412 qualitatively similar to CB1, with the exception that the nucleation sites appeared to be different.
413 For CB2 the compaction appeared to nucleate from near the central region (Fig. 8c) and spread
414 sideways (Fig. 8d), whereas for CB3, it initiated near the center and left side (Fig. 9c), and then
415 spread towards the right (Fig. 9d).



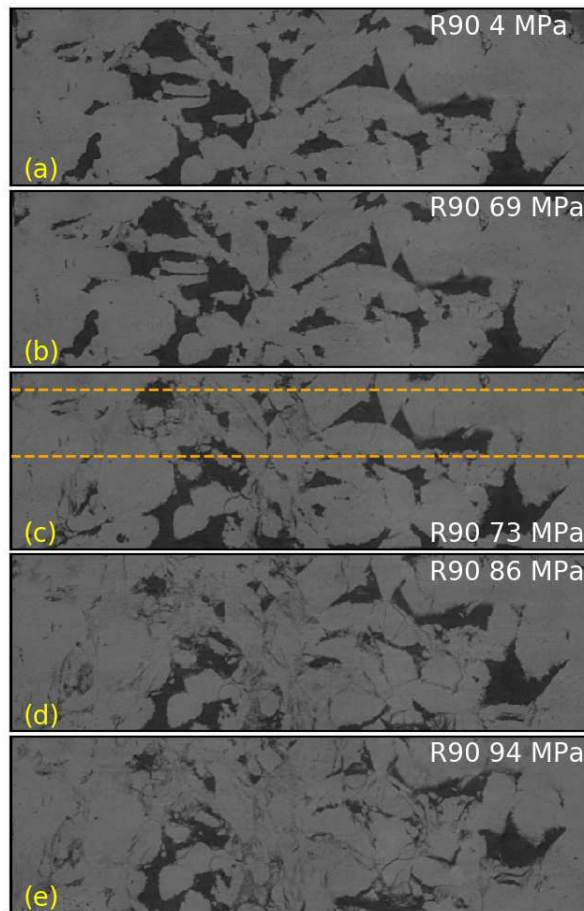
416
417
418
419
420

Fig. 7. (a-e) Five micrographs of CB1 acquired at different levels of stress marked in inset of Fig. 1. The width of the micrographs is 4.55 mm. A band of damage is indicated by an arrow in Fig. 7e.



421
422
423
424

Fig. 8. (a-e) Five micrographs of CB2 acquired at different levels of stress marked in inset of Fig. 1. The width of the micrographs is 4.55 mm.



425
 426 **Fig. 9.** (a-e) Five micrographs of CB3 acquired at different levels of stress marked in inset of
 427 Fig. 1. The width of the micrographs is 4.55 mm
 428

429 **4. Discussion**

430 In this study we conducted a triaxial compression experiment on Leitha limestone in an
 431 apparatus that is transparent to the X-ray fluxes of a synchrotron source. With a spatial resolution
 432 of 6.5 μ m, 4D imaging of the sample has allowed us to effectively characterize the progressive
 433 development of failure at multiple scales ranging from that of the sample down to the grain.
 434 Unlike previous studies that tackled this by imaging deformed samples after multiple loading
 435 cycles (e.g., Baud et al., 2015), which is time-consuming and subject to microstructural artifacts

436 from sample unloading, here the research objectives were fully accomplished in one single
437 experiment. In our limestone the mechanical deformation evolved in two stages of yielding
438 manifested by fundamentally different mechanisms. Because the failure did not involve any
439 strain softening or dynamic instability, we were able to elucidate details of its complex
440 development as the sample deformed quasi-statically. To our knowledge this is the first study
441 that has successfully captured using 4D synchrotron X-ray imaging the quasi-static development
442 of compaction strain localization and then failure from the grain to continuum scale in a highly
443 porous carbonate representative of geological reservoir rocks.

444 *4.1. Two stages of yielding in a rock with strong heterogeneity of porosity*

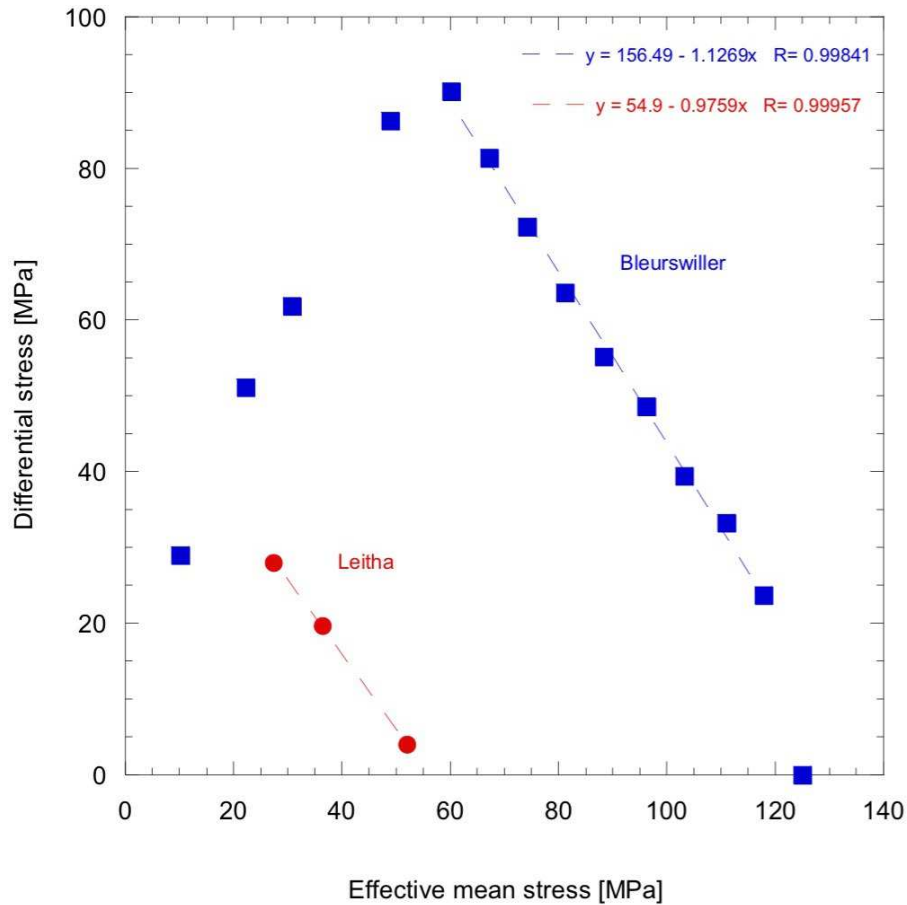
445 Our analysis of strain partitioning at the mesoscopic scale (Fig. 4) indicates that the first and
446 second stages of yielding were associated with distributed and localized compactions in the
447 upper and lower parts of the sample, respectively. The initial yield stress C^* marks the onset of
448 the collapse of a cluster of macropores in the top layer (Fig. 6). It is of interest to note that Baud
449 et al. (2015) inferred a similar behavior in Bleurswiller sandstone, the pore space of which was
450 also highly heterogeneous. They proposed that the initial yield of such a rock would typically
451 involve the collapse of an anomalously porous region, and they furthermore developed a
452 micromechanical model that predicts the initial yield envelope can be approximated by a linear
453 cap. Analogous to our observations here, it was only after the first stage of yielding and the pore
454 space had been homogenized somewhat by the pore collapse that the Bleurswiller sandstone
455 sample progressed to the second yield C^{**} , when discrete compaction bands developed.

456 In their model for initial yield, Baud et al. (2015) analyzed the onset of pore collapse for the
457 idealized case of a spherical pore embedded in a matrix that fails according to the Coulomb
458 criterion. For a dry sample under axisymmetric loading, the yield stress can be expressed as:

459

$$Q = \frac{3(7-5\nu)}{10(2-\nu)}(P^* - P) \quad (1)$$

460 where Q is the differential stress, P the mean stress, P^* the pressure for the onset of pore collapse
461 under hydrostatic loading, and ν Poisson's ratio. According to Equation (1), the compactant yield
462 envelope in the P-Q space is linear with a slope close to 1 for standard values of Poisson's ratio.
463 To better constrain the initial yield envelope of Leitha limestone for comparison with this model,
464 we performed two additional experiments on dry samples cored from the same block as our
465 sample deformed at the synchrotron. These samples were of larger size (40 mm length and 20
466 mm in diameter). One sample was loaded in conventional triaxial compression at 30 MPa of
467 confining pressure, and the other at a constant differential stress of 4 MPa, following a procedure
468 detailed in Cilona et al. (2014). The mechanical data are presented in Fig. S5, and published
469 mechanical data on compactant yield in porous rocks do not indicate any systematic sample size
470 effects (see for example Tembe et al., 2008). The two new data points bracket the C^* value for
471 our synchrotron experiment (Fig. 1), and altogether the three yield stresses fall on a linear trend
472 with a slope close to 1 (Fig. 10), in agreement with model prediction (1) for $\nu = 0.2$. For
473 reference we include in the figure the corresponding yield envelope and previous data of Baud et
474 al. (2015) on Bleurswiller sandstone, which motivated the elastic-plastic pore collapse model.
475 That this model has been demonstrated to be applicable to porous sandstone and limestone with a
476 relatively heterogeneous pore space suggests that it may be valid for a broad range of porous
477 rocks such similar preexisting heterogeneities in their pore spaces.



478
 479 **Fig. 10.** Comparison between the yield envelopes of Leitha limestone (red circles) and
 480 Bleurswiller sandstone (blue squares) from Baud et al. (2015), plotted in the differential
 481 stress-effective mean stress space. Linear fits are shown as dashed lines for both envelopes.
 482

483 *4.2. Time-lapse imaging of the dynamics of compaction band formation*

484 Our current understanding of the micromechanics of strain localization derives primarily
 485 from AE location and microstructural observation. The former has the intrinsic limitation of
 486 being basically kinematic in nature, whereas the latter typically involves post-mortem
 487 characterization of damage on multiple samples, which can be difficult to distinguish from
 488 artifacts of unloading and sample-to-sample variations. To our knowledge, this is the first study
 489 that has circumvented these limitations and successfully captured in details the spatiotemporal
 490 evolution of damage related to the dynamics of compaction band formation.

491 On a continuum scale the dynamics of compaction localization is approximated as a
492 bifurcation phenomenon associated with constitutive instability. On the grain scale, a number of
493 computational micromechanical models (e.g., Wang et al., 2008) have been adopted to predict
494 how the strain localization would initiate and propagate. Our voxel-scale images (Fig. 7, 8, and
495 9) provide the first time-lapse microstructural observations of the micromechanics of the
496 initiation and propagation of CB formation. As we have shown, the presence of large
497 heterogeneities had a strong impact on the development of stress induced damage in Leitha
498 limestone, particularly in our relatively small sample. It is clear that the presence or absence of
499 such of large heterogeneities would constrain the position of the compaction bands and
500 numerical modelling would need to integrate such complexity to reproduce the results presented
501 here. Here we have focused on the radiographs, but the logical next step is to analyze the 3D
502 complexity of damage development and dynamics of compaction localization using the full set
503 of μ CT images and Digital Image Correlation (Renard et al., 2019). An example of such
504 complexity resembles a scenario obtained by Tran et al. (2019) in a rock-like porous material
505 using Digital Image Correlation in which an episode of compaction banding was followed by
506 shear banding.

507 *4.3. Compaction localization and time dependent compaction in porous limestone*

508 Since CBs were first observed in sandstone formations, considerable efforts have been
509 made to reproduce such structures in laboratory samples, because of the potential implications
510 for fluid flow at various scales. Series of experimental studies (Baud et al., 2004; Fortin et al.,
511 2005) were successful in producing CBs in cm-size samples. Further analysis revealed that the
512 geometric attributes of field and laboratory CBs follow the same scaling law (Tembe et al., 2008),
513 and that the grain size distribution and porosity are in both cases the key parameters controlling

514 the nucleation of CBs in sandstone (Cheung et al., 2012), in agreement with the discrete element
515 modeling of Wang et al. (2008).

516 Despite the increasing number of field evidence of CBs in limestone formations and of
517 laboratory studies on carbonates, a similar consensus has yet to emerge as far as the occurrence
518 of CBs in porous carbonates is concerned. Laboratory studies showed clearly that compaction
519 localization can occur in limestone (Ji et al., 2015; Baud et al., 2017a), but the link with field
520 observations remains ambiguous. In fact, since field CBs in limestone are often associated with
521 pressure-solution seams (see for example Tondi et al., 2006), one postulate is that chemical
522 processes would be needed to trigger the nucleation of CBs in limestone. In this study, we show
523 unequivocally that this is not the case at least for Leitha limestone. Our 4D μ CT data have
524 elucidated the dynamical development of multiple discrete CBs in a dry carbonate. As in
525 sandstone, pore collapse and grain crushing were the main mechanisms that trigger the
526 development of compaction localization.

527 Leitha limestone could be seen as an end-member type of carbonate because this rock is
528 mostly macroporous (Baud et al., 2017a) and its microstructure is somehow similar to that of
529 some sandstones. An outstanding question for future studies would be whether comparable CBs
530 could develop in limestone with dual porosity. This is a difficult challenge since a large part of
531 the pore space would not be visible even at the high resolution used in this study.

532 4D imaging of stress-induced damage in rock based on the method used in this study
533 presents some other limitations beyond resolution related issues. Such technique would not really
534 be efficient if the deformation would occur too fast (because of the incompressible duration of
535 the scans), too slow because of obvious limitations on available beam time, but also if significant
536 time-dependent deformation (creep) would occur during the scanning process. Since previous

537 studies reported time-dependent deformation in limestone (e.g. Brantut et al., 2014), we decided
538 to perform our experiment in dry conditions. Even so, we observed some creep at several levels
539 of stress, in particular at about 17 MPa of differential stress (Fig. S4). These data show some
540 notable similarities with the creep data on Bleurswiller sandstone presented by Heap et al. (2015).
541 At constant stress (creep conditions), the strain rate decreased but the data were punctuated by
542 episodic changes in strain rate, an indicator of compaction localization. Based on the results of
543 Heap et al. (2015), we can speculate that significant time-dependent compaction driven by stress-
544 corrosion microcracking is also expected in Leitha limestone at stress levels beyond C^* . Existing
545 studies on stress corrosion and creep (Atkinson and Meredith, 1987; Brantut et al., 2013) suggest
546 that the resulting strain rates would be strongly influenced in particular by the presence of fluid,
547 fluid chemistry and temperature. In the presence of fluid, CBs could therefore develop in the
548 field at much lower stresses over extended periods of time. At these time scales, other chemical
549 processes should also contribute to the evolution of CB's microstructure.

550

551 **5. Conclusion**

552 We used *in situ* dynamic synchrotron X-ray imaging to study in real time the
553 development of stress-induced damage associated with inelastic compaction and failure in a
554 porous limestone. Leitha limestone was selected for this study because its pore space is
555 dominated by relatively large macropores with optimum size. Most of the pore space could
556 therefore be resolved in our high resolution images, and no filtering or image analysis was
557 necessary to infer the evolution of the global and local porosity.

558 To our knowledge this is the first study that has successfully captured the quasi-static
559 development of failure and strain localization from the grain to continuum scale in a limestone
560 reservoir rock. Several conclusions could be drawn from our results:

561 1) Discrete CBs can develop in a porous limestone, even in dry conditions. The μ CT data at the
562 voxel scale elucidate in refined details the nucleation and propagation of discrete CBs under
563 quasi-static loading. The development of CBs involves grain crushing and pore collapse, both
564 visible in our μ CT images beyond the yield point.

565 2) Inelastic compaction of Leitha limestone is characterized, as in some sandstones, by a double
566 yielding behavior. At the onset of shear-enhanced compaction C^* , our μ CT images revealed
567 mostly cataclastic pore collapse, while the second yield stress C^{**} was associated with onset of
568 bifurcation and development of discrete CBs.

569 3) Time-dependent compaction and time-dependent compaction band growth were observed
570 during part of our experiment performed in dry conditions. In the field, CBs could therefore
571 potentially grow in limestone at relatively low stresses over extended period of time.

572

573 **Acknowledgements**

574 We are most grateful to Ulrike Exner for helping with the sample collection and thank two
575 reviewers whose suggestions greatly improved the manuscript. This study was partially funded
576 by the Hong Kong Research Grants Council GRF 14305714 and GRF14323916, the France-
577 Hong Kong Collaborative Program Procore 30805PM and F-CUHK405/16, the Norwegian
578 Research Council (grant 250661), and CNRS (PICS grant 07961). Beamtime was allocated at the

579 European Synchrotron Radiation Facility (Long Term Proposal ES-295). Data storage was
580 provided by UNINETT Sigma2 (project NS9073K). The X-ray tomography data will be made
581 available to the scientific community at <https://archive.norstore.no/> upon acceptance of the
582 article (Renard, 2019).

583

584 **References**

585 Anders, M.H., Laubach, S.E., Scholz, C.H., 2014. Microfractures: A review. *J. Struct. Geol.* 69,
586 377-394.

587 Andò, E., Hall, S.A., Viggiani, G., Desrues, J., Bésuelle, P., 2012. Grain-scale experimental
588 investigation of localised deformation in sand: a discrete particle tracking approach. *Acta*
589 *Geotechnica* 7 (1), 1-13.

590 Atkinson, B.K., Meredith, P.G., 1987. Experimental fracture mechanics data for rocks and
591 minerals, in *Fracture Mechanics of Rock*, edited by B. K. Atkinson, pp. 477-525, Academic
592 Press, London.

593 Baud, P., Exner, U., Lommatzsch, M., Reuschlé, T., Wong, T.-f., 2017a. Mechanical behavior,
594 failure mode, and transport properties in a porous carbonate. *J. Geophys. Res., Solid Earth* 122
595 (9), 7363–7387.

596 Baud, P., Schubnel, A., Heap, M.J., Rolland, A., 2017b. Inelastic compaction in high-porosity
597 limestone monitored using acoustic emissions. *J. Geophys. Res., Solid Earth* 122 (12), 9989-
598 10,008.

599 Baud, P., Reuschlé, T., Ji, Y., Cheung, C.S.N., Wong, T.-f., 2015. Mechanical compaction and
600 strain localization in Bleurswiller sandstone. *J. Geophys. Res., Solid Earth* 120 (9), 6501–6522.

601 Baud, P., Meredith, P.G., Townend, E., 2012. Permeability evolution during triaxial compaction
602 of an anisotropic porous sandstone. *J. Geophys. Res. Solid Earth* 117 (B5), B05203.

603 Baud, P., Klein, E., Wong, T.-f., 2004. Compaction localization in porous sandstones: Spatial
604 evolution of damage and acoustic emission activity. *J. Struct. Geol.* 26 (4), 603–24.

605 Brantut, N., Heap, M.J., Baud, P., Meredith, P.G., 2014. Mechanisms of time-dependent
606 deformation in porous limestone. *J. Geophys. Res., Solid Earth* 119 (7), 5444-5463.

607 Brantut, N., Heap, M.J., Meredith, P.G., Baud, P., 2013. Time-dependent cracking and brittle
608 creep in crustal rocks. *J. Struct. Geol.* 52, 17-43.

609 Baxevanis, T., Papamichos, E., Flornes, O., Larsen, I., 2006. Compaction bands and induced
610 permeability reduction in Tuffeau de Maastricht calcarenite. *Acta Geotech.* 1 (2), 123–35.

611 Cheung, C., Baud, P., Wong, T.-f., 2012. Effect of grain size distribution on the development of
612 compaction localization in porous sandstone. *Geophys. Res. Lett.*, 39, L21302.

613 Eichhubl, P., Hooker, J.N., Laubach, S.E., 2010. Pure and shear-enhanced compaction bands in
614 Aztec sandstone. *J. Struct. Geol.* 32 (12), 1873–86.

615 Fortin, J., Stanchits, S., Dresen, G., Guéguen, Y., 2006. Acoustic emission and velocities
616 associated with the formation of compaction bands in sandstone. *J. Geophys. Res., Solid Earth*
617 111 (B10), B10203.

618 Fortin, J, Schubnel, A., Guéguen, Y., 2005. Elastic wave velocities and permeability evolution
619 during compaction of Bleurswiller sandstone. *Int. J. Rock Mech. Min. Sci.* 42 (7-8), 873–89.

620 Fossen, H., Soliva, R., Ballas, G., Trzaskos, B., Cavalcante, C., Schultz, R.A., 2017. A review of
621 deformation bands in reservoir sandstones: geometries, mechanisms and distribution. From:
622 Ashton, M., Dee, S. J. & Wennberg, O. P. (eds) *Subseismic-Scale Reservoir Deformation*. Geol.
623 Soc., London, Special Publications, 459, <https://doi.org/10.1144/SP459.4>.

624 Fossen, H., Schultz, R.A., Torabi, A., 2011. Conditions and implications for compaction band
625 formation in the Navajo sandstone, Utah. *J. Struct. Geol.* 33 (10), 1477–90.

626 Fousseis, F., Steeb, H., Xiao, X., Zhu, W., Butler, I. B., Elphick, S., Mäder, U., 2013. A low-cost
627 X-ray-transparent experimental cell for synchrotron-based X-ray microtomography studies under
628 geological reservoir conditions, *J. Synchrotron Rad.*, 21, 251-253.

629 Heap, M.J., Brantut, N., Baud, P., Meredith, P.G., 2015. Time-dependent compaction band
630 formation in sandstone. *J. Geophys. Res., Solid Earth* 120 (7) 4808–4830.

631 Ji, Y., Hall, S.A., Baud, P., Wong, T.-f., 2015. Characterization of pore structure and strain
632 localization in Majella limestone by X-ray computed tomography and digital image correlation,
633 *Geophys. J. Int.* 200, 701-719.

634 Ji, Y., Baud, P., Vajdova, V., Wong, T.-f., 2012. Characterization of pore geometry of Indiana
635 limestone in relation to mechanical compaction. *Oil & Gas Science and Technology–Revue de*
636 *l’IFP Energies Nouvelles* 67 (5), 753–75.

637 Lenoir, N., Bornert, M., Desrues, J., Bésuelle, P., Viggiani, G., 2007. Volumetric Digital Image
638 Correlation applied to X-ray microtomography images from triaxial compression tests on
639 argillaceous rock. *Strain* 43 (3), 193–205.

640 Lockner, D.A., Byerlee, J.D., Kuksenko, V., Ponomarev, A., Sidorin, A., 1992. Observations of
641 quasistatic fault growth from acoustic emissions. In *Int. Geophys.* 51, 3–31.

642 Louis, L., Wong, T.-f., Baud, P., Tembe, S., 2006. Imaging strain localization by X-ray
643 Computed Tomography: Discrete compaction bands in Diemelstadt sandstone. *J. Struct. Geol.* 28
644 (5), 762–775.

645 Mirone, A., Brun, E., Gouillart, E., Tafforeau, P., Kieffer, J., 2014. The Pyhst2 hybrid distributed
646 code for high speed tomographic reconstruction with iterative reconstruction and a priori
647 knowledge capabilities. *Nuclear Instruments and Methods in Physics Research Section B: Beam
648 Interactions with Materials and Atoms* 324, 41–48.

649 Mollema, P.N., Antonellini, M.A., 1996. Compaction bands: A structural analog for anti-mode I
650 cracks in aeolian sandstone. *Tectonophysics* 267 (1-4), 209–228.

651 Moore, D.E., Lockner, D.A., 1995. The role of microcracking in shear-fracture propagation in
652 granite. *J. Struct. Geol.* 17 (1), 95–114.

653 Olsson, W.A., Holcomb, D.J., 2000. Compaction localization in porous rock. *Geophys. Res. Lett.*
654 27 (21). Wiley Online Library: 3537–40.

655 Olsson, W.A. 1999. Theoretical and experimental investigation of compaction bands in porous
656 rock. *J. Geophys. Res., Solid Earth* 104 (B4), 7219–7228.

657 Passchier, C.W., Trouw, R.A.J., 2005. *Microtectonics*. Springer Science & Business Media.

658 Paterson, M.S., Wong, T.-f., 2005. *Experimental rock deformation-the brittle field*. Springer
659 Science & Business Media.

660 Rath, A., Exner, U., Tschegg, C., Grasemann, B., Laner, R., Draganits, E., 2011. Diagenetic
661 control of deformation mechanisms in deformation bands in a carbonate grainstone. *AAPG*
662 *Bulletin* 95 (8), 1369–1381.

663 Renard, F., (2019). Synchrotron X-ray imaging in 4D: Multiscale failure and compaction
664 localization in triaxially compressed porous limestone [Data set]. Norstore.
665 <https://doi.org/10.11582/2019.00015>.

666 Renard, F., McBeck, J., Cordonnier, B., Zheng, X., Kandula, N., Sanchez, J.R., Kobchenko, M.,
667 Noirel, C., Zhu, W., Meakin, P., Fousseis, F., Dysthe, D.K., 2019. Dynamic in situ three-
668 dimensional imaging and digital volume correlation analysis to quantify strain localization and
669 fracture coalescence in sandstone. *Pure and applied Geophysics* 176 (3), 1083-1115.

670 Renard, F., Cordonnier, B., Kobchenko, M., Kandula, N., Weiss, J., Zhu, W., 2017. Microscale
671 characterization of rupture nucleation unravels precursors to faulting in rocks. *Earth Planet. Sci.*
672 *Lett.* 476, 69-78, doi: 10.1016/j.epsl.2017.08.002.

673 Renard, F., Cordonnier, B., Dysthe, D.K., Boller, E., Tafforeau, P., Rack, A., 2016. A
674 deformation rig for synchrotron microtomography studies of geomaterials under conditions down
675 to 10 Km depth in the earth. *J. Synchrotron Rad.* 23 (4), 1030–1034.

676 Rudnicki, J.W., 2004. Shear and compaction band formation on an elliptic yield cap. *J. Geophys.*
677 *Res., Solid Earth* 109 (B3), B03402, 1-10.

678 Schubnel, A., Benson, P.M., Thompson, B.D., Hazzard, J.F., Young, R.P., 2006. Quantifying
679 damage, saturation and anisotropy in cracked rocks by inverting elastic wave velocities. In *Rock*
680 *Damage and Fluid Transport, Part I*, 947–73. Springer.

681 Sternlof, K.R., Chapin, J.R., Pollard, D.D., Durlofsky, L.J., 2004. Permeability effects of
682 deformation band arrays in sandstone. *AAPG Bulletin* 88 (9), 1315–1329.

683 Tembe, S., Baud, P., Wong, T.-f., 2008. Stress conditions for the propagation of discrete
684 compaction bands in porous sandstone. *J. Geophys. Res., Solid Earth* 113 (B9), B09409.

685 Tondi, E., Antonellini, M.A., Aydin, A., Marchegiani, L., Cello G., 2006. The role of
686 deformation bands, stylolites and sheared stylolites in fault development in carbonate grainstones
687 of Majella Mountain, Italy. *J. Struct. Geol.* 28, 376-391.

688 Townend, E., Thompson, B.D., Benson, P.M., Meredith, P.G., Baud, P., Young, R.P., 2008.
689 Imaging compaction band propagation in Diemelstadt sandstone using acoustic emission
690 locations. *Geophys. Res. Lett.* 35 (15), L15301.

691 Tran, T.-P.-H., Bouissou, S., Chemenda, A., Ambre, J., Vacher, P., Michel, P., 2019. Initiation
692 and evolution of a network of deformation bands in a rock analogue material at brittle-ductile
693 transition. *Rock Mech. Rock Eng.*, 52(3), 737-752.

694 Vajdova, V., Baud, P., Wong, T.-f., 2004. Permeability evolution during localized deformation
695 in Bentheim sandstone. *J. Geophys. Res., Solid Earth* 109 (B10), B10406, 1-15.

696 Wang, B., Chen, Y., Wong, T.-f., 2008. A discrete element model for the development of
697 compaction localization in granular rock. *J. Geophys. Res., Solid Earth*, 113, B03202,
698 doi:03210.01029/02006JB004501.

699 Wong, T.-f., Baud, P., 2012. The brittle-ductile transition in porous rock: A Review. *J. Struct.*
700 *Geol.* 44, 25–53.

701 Wong, T.-f., Baud, P., Klein, E., 2001. Localized failure modes in a compactant porous rock.
702 *Geophys. Res. Lett.* 28 (13), 2521–2524.

703 Wong, T.-f., 1982. Micromechanics of faulting in Westerly granite. *Int. J. Rock Mech. Min. Sci.*
704 *Geomechanics Abstracts* 19, 49–64.

705 Zang, A., Wagner, F.C., C., Stanchits, S., Janssen, C., Dresen, G., 2000. Fracture process zone in
706 granite. *J. Geophys. Res., Solid Earth* 105 (B10), 23651–23661.

707 Zhao, Q., Tisato, N., Kovaleva, O., Grasselli, G., 2018. Direct observation of faulting by means
708 of rotary shear tests under X - ray micro - computed tomography. *J. Geophys. Res.: Solid Earth*
709 123 (9), 7389-7403.